Application of the NARCM model to high-resolution aerosol simulations: Case study of Mexico City basin during the Investigación sobre Materia Particulada y Deterioro Atmosférico-Aerosol and Visibility Research measurements campaign

Rodrigo Munoz-Alpizar and Jean-Pierre Blanchet
Department of Earth and Atmospheric Sciences, University of Quebec at Montreal, Montreal, Quebec, Canada

Arturo I. Quintanar
Instituto Mexicano del Petroleo, Mexico D. F., Mexico

Received 24 October 2002; revised 31 March 2003; accepted 24 April 2003; published 9 August 2003.

[1] The Northern Aerosol Regional Climate Model (NARCM) is used to study the visibility and three-dimensional (3-D) evolution of aerosol distributions within the Mexico City basin. NARCM simulates transport, diffusion, deposition, and size distributions of sulphur aerosol particles in the region. The model assumes only simple sulphur oxidation, not taking explicitly into account the urban air chemistry. Rather, it focuses on detailed aerosol microphysics and 3-D optical properties. The simulation performance is compared with upper air and ground-based observations for the following specific days of intensive measurement: 2, 4, and 14 March 1997. Time series at Mexico City airport shows lower values of visibility in the morning due to a shallow mixed layer and higher values in the afternoon following the evolution of the mixed layer depth. Modeled visibility shows large dependence on cardinal direction and size distribution of particles. It is found that better resolution of particle size leads to better representation of coagulation processes and to realistic size distributions which show a characteristic accumulation mode around 0.3 μm. As a result, visibility simulations are closer to those observed at the airport location. Comparing visibility is a stringent test for the model because it requires an accurate representation of 3-D meteorological fields together with a realistic aerosol simulation. *INDEX TERMS:* 0305 Atmospheric Composition and Structure: Aerosols and particles (0345, 4801); 0345 Atmospheric Composition and Structure: Pollution—urban and regional (0305); 3329 Meteorology and Atmospheric Dynamics: Mesoscale meteorology; *KEYWORDS:* aerosols, visibility, transport, sulphate

Citation: Munoz-Alpizar, R., J.-P. Blanchet, and A. I. Quintanar, Application of the NARCM model to high-resolution aerosol simulations: Case study of Mexico City basin during the Investigación sobre Materia Particulada y Deterioro Atmosférico-Aerosol and Visibility Research measurements campaign, *J. Geophys. Res.*, *108*(D15), 4462, doi:10.1029/2002JD003074, 2003.

1. Introduction

[2] The largest contribution to anthropogenic emissions comes from urban sources which emit a large variety of gaseous and particulate species [*Seinfeld and Pandis*, 1998]. The Mexico City metropolitan area (MCMA) is an important example of how these emissions affect vegetation, wildlife, and human health [*Borja-Aburto et al.*, 1997; *Romieu et al.*, 1999] and alter regional climate [*Raga et al.*, 2001]. Improving air quality has been a priority for federal and local government agencies during the last decade; unfortunately visibility degradation in the MCMA continues to be a major problem.

[3] The MCMA lies in a basin ~(18–20°N, 98–100°W) at an elevation of 2240 m above sea level. Except to the north, it is surrounded by mountains rising an additional 1200 m, creating a barrier to air circulation and isolating the area from the winds of regional weather pattern. The complex topography of the MCMA contributes to the formation of an urban heat island [*Jauregui*, 1988, 1997]. The local air circulations control the transport and the dispersion of pollutants in the region [*Fast and Zhong*, 1998]. During the morning, cold air drains off the mountain slopes, resulting in nearly stagnant air over the city [*Oke et al.*, 1992]. After sunrise the southwest mountain slopes of the MCMA are heated. Winds tend to blow across the MCMA from the northeast, bringing moisture from the Gulf of Mexico into the basin [*Fast and Zhong*, 1998]. This wind also brings pollution from the heavily industrialized northern MCMA toward the city center and the southwestern suburban area.

[4] The high altitude of the basin reduces the mass concentration of oxygen and favors ozone production. This condition also affects the efficiency of combustion in motor

0148-0227/03/2002JD003074

vehicles which produce twice as much carbon monoxide and hydrocarbon emissions than those found at sea level [*Collins and Scott*, 1993].

[5] In order to characterize air pollution within the MCMA, several field experiments have been designed and carried out in collaboration with national and international agencies. One such effort was the Mexico City Air Quality Research Initiative (MARI) conducted during the winters of 1990–1993 jointly by the Instituto Mexicano del Petróleo (IMP) and the Los Alamos National Laboratory [*Guzman and Streit*, 1993]. During the spring of 1997, another more complete and intensive field campaign was performed, named Investigación sobre Materia Particulada y Deterioro Atmosférico-Aerosol and Visibility Research (IMADA-AVER) [*Doran et al.*, 1998]. The IMADA-AVER campaign included measurements of three-dimensional (3-D) meteorological fields and surface air quality within the MCMA.

[6] Meteorological processes responsible for inhomogeneous ozone concentrations in the region were investigated by *Fast and Zhong* [1998] and *Edgerton et al.* [1999] using data from the IMADA-AVER campaign. Ozone measurements made throughout the MCMA over the past several years have shown that ozone concentrations are usually highest in the southwest section of the city and lowest in the northeast [*Doran et al.*, 1998].

[7] The main goal of this study is to describe the meteorological processes and the 3-D distribution of aerosol in the region, in order to understand how emissions from various sources affect visibility throughout the city. To this end, the Northern Aerosol Regional Climate Model (NARCM) is used throughout the MCMA to treat the microphysical and optical properties of aerosols on a physical basis. Although NARCM was mostly intended for large regional and global scales [*von Salzen et al.*, 2000; *Gong et al.*, 2003], the governing equations are general enough to be applied to kilometer-scale resolutions. To gain confidence on the meteorological simulations, 3 days with high ozone concentrations were chosen for high-resolution NARCM simulations. These particular days have also been the subject of recent studies performed with the Regional Atmospheric Modeling System (RAMS) [see *Whiteman et al.*, 2000, and references therein].

[8] Admittedly, a fully coupled aerosol-chemistry model is required to simulate the complete air quality-climate problem. This study, however, takes a first step toward investigating the interplay between 3-D optics, aerosol microphysics, and regional-scale circulation in the MCMA.

2. Methodology

[9] The IMADA-AVER field campaign was designed to capture most of the basin-scale circulation patterns; however, the observational data are insufficient to describe in detail both the 3-D circulation and the characteristics of urban emissions within the basin. Thus observations at individual sites may not be representative over a large area due to the complexity of the terrain and the lack of horizontal resolution of the observational network. In order to complement the observational data and to gain further insight into the mechanisms that force and maintain local circulations, numerical models are used to assimilate the local observational data and downscaling of the large-scale fields [*Georgi*, 1990; *Caya and Laprise*, 1999; *Fast and Zhong*, 1998; *Whiteman et al.*, 2000].

[10] On the other hand, the effect of the time-dependent 3-D wind field on aerosols distribution within the MCMA is not well understood, and information about the physical and optical properties of the MCMA aerosols is sparse. In that context a detailed spatial and temporal model description of aerosol evolution is required to begin understanding some of the main processes that constitute air quality and visibility impairment in the MCMA. Here we use NARCM during three well-documented high-ozone days of the IMADA-AVER field campaign [*Fast and Zhong*, 1998].

2.1. Meteorological Measurements

[11] The IMADA-AVER campaign [*Doran et al.*, 1998] took place from 23 February to 22 March 1997. The field campaign experiment included four 915-Mhz radar profilers located at Cuautitlan, Teotihuacán, Universidad Nacional Autónoma de México (UNAM), and Chalco (Figure 1) that provided hourly vertical wind profiles up to 4 km above ground level (AGL). To describe the development of the boundary layer structure within the basin, temperature and humidity profiles were obtained from radiosondes released five times per day at the same locations. Although not used in this study, these measurements were supplemented by sodars at Cuautitlan and Teotihuacán and radiosondes released at Tres Marias and Pachuca outside of the MCMA.

2.2. Aerosol and Visibility Measurements

[12] Air quality measurements were acquired from 33 automated surface monitoring stations of the metropolitan Red Automatica de Monitoreo Atmosférico (RAMA) network under the city government administration. This network provided hourly near-surface measurements of ozone, carbon monoxide, sulphur dioxide, nitrogen oxides, and fine particulate. Nineteen RAMA sites measuring near-surface ozone, 8 measuring particulate matter (PM_{10}) concentrations, and 10 measuring meteorological variables were used (Figure 1).

[13] Only one station located at Mexico City's Benito Juarez International Airport (19.438°N, 99.078°W, 2231 m ASL) is available for visibility data. These observations were made hourly by specially trained personnel, per procedures established by the World Meteorological Organization. At this station, visibility at any one point is the result of several horizontal integrated paths that account for the variation of particulate concentration, refractive index, wavelength, size distribution, and direction. Visibility values are on the order of a few tens of kilometers, and therefore this single station is representative of a sufficiently large area, adequate for verification and demonstration purposes.

3. Model Description

[14] NARCM is the basic atmospheric modeling system and tool used in this study. It is composed of several dynamical and physical modules that account for advective transport and diffusion of passive scalars, cloud processes, radiation-aerosol interactions, and a simplified chemistry

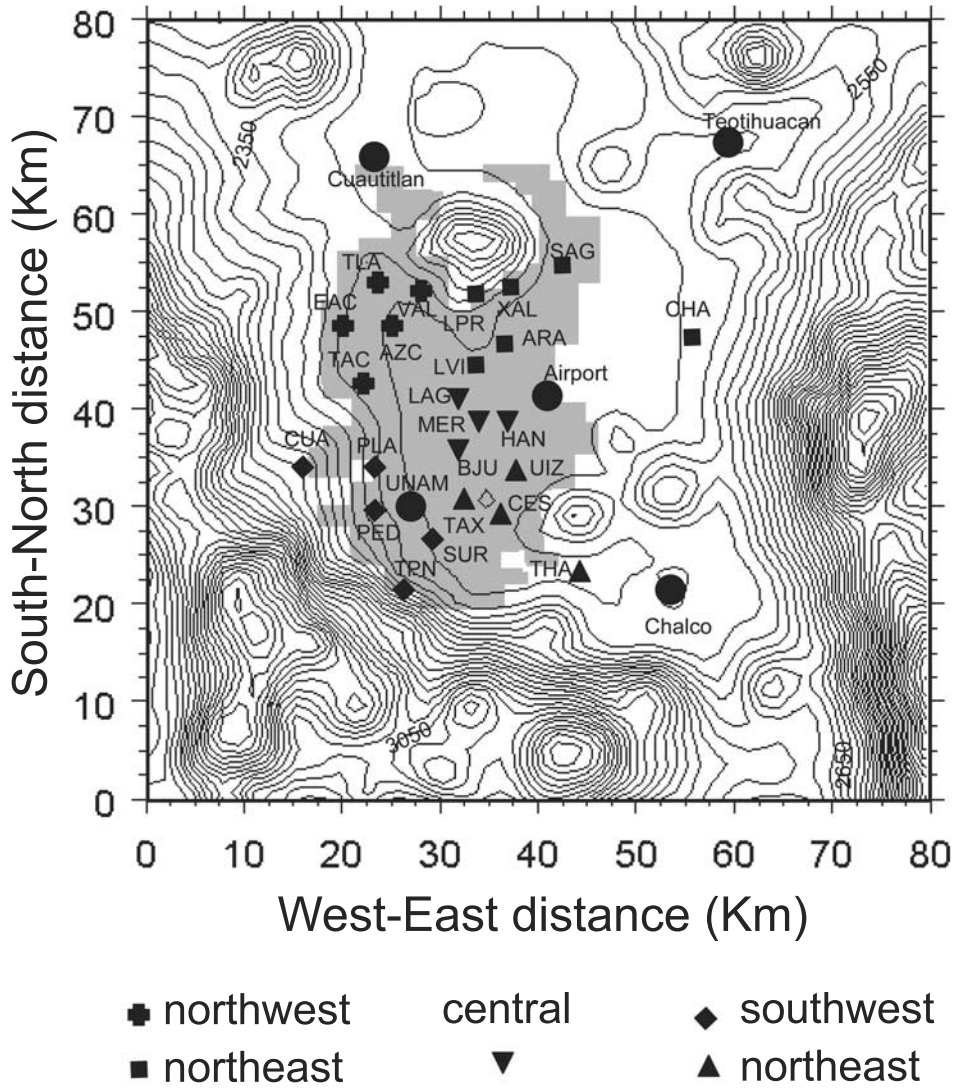

Figure 1. Topography of the Mexico City metropolitan area (MCMA) (50-m contour interval) and its surroundings show locations of the four 915-MHz radar wind profiler and radiosonde sites (solid circles). Shaded area marks approximate the bounds of the MCMA. The symbols denote the locations of five sets of RAMA monitoring near-surface stations that measure ozone, meteorological variables, and PM_{10}.

module. In addition, a module that computes optical properties of the atmosphere is included.

3.1. Meteorological Model

[15] The meteorological module of NARCM (L. Spacek et al., unpublished manuscript, 1999) is a limited area nonhydrostatic dynamical model identical in every respect to the Canadian Regional Climate Model (CRCM) [*Laprise et al.*, 1997; *Caya and Laprise*, 1999]. It is based on the fully elastic, nonhydrostatic Euler equations solved with semi-implicit and semi-Lagrangian marching schemes. A physical parameterization package imported from the Canadian General Circulation Model (CGCM) [*McFarlane et al.*, 1992; *Zhang and McFarlane*, 1995] is used by NARCM. The parameterization package takes into account the following processes: radiation, gravity wave drag, turbulent diffusion, surface processes, and convective clouds. In addition, surface processes are taken into account with the Canadian Land Surface Scheme (CLASS) [*Verseghy*, 1991; *Verseghy et al.*, 1993]. NARCM employs a bulk model to represent cumulus clouds mixing including the effects of entrainment and detrainment on the updraft and downdraft convective mass fluxes [*Zhang and McFarlane*, 1995].

[16] The meteorological module of NARCM includes an initialization procedure for the computational domain driven by National Centers for Environmental Prediction (NCEP) reanalysis [*Yakimiw and Robert*, 1990]. Nudging to the NCEP data is performed in a nine-point sponge zone next to the lateral boundaries, and throughout the rest of the computational domain the variables of the regional model are not affected by the nudging technique [*Caya and Laprise*, 1999]. One-way nesting is carried out to high-resolution domains once the variables have been dynamically updated. Thus NARCM is expected to generate its own high-resolution weather and climate from information provided at the lateral boundaries only. The ability of the model to regenerate fine-scale features of the meteorological fields

within the nested domains has been studied in detail by *Denis et al.* [2003]. Here we note the difference in the nudging and initialization procedures with other area-limited regional models such as RAMS and the Penn State University/National Center for Atmospheric Research mesoscale model (MM5) which extend the nudging to the inner nested grids and allow information to feedback to the coarse resolution grids (two-way nesting).

3.2. Aerosol Model

[17] The physical and chemical processes that determine the aerosol compositions and size distributions in NARCM are determined by the Canadian Aerosol Model (CAM) [*Gong et al.*, 2003]. In the model, SO_2 is mainly emitted from industrial sources on the continents. A small fraction of SO_2 may also be produced by gas phase reactions of hydrogen sulfide (H_2S) and dimethylsulfide (DMS) from natural sources with the hydroxyl radical (OH) and the nitrate radical (NO_3) (Spacek et. al., unpublished manuscript, 1999).

[18] The current version of NARCM includes five species (sulphate, soot, soil, sea salt, and organics). Organics in the form of black and organic carbon were excluded from the calculations since no reliable emission inventories of organic compounds for the whole MCMA during the IMADA-AVER campaign were available [*Molina and Molina*, 2000]. Also, sea salt does not contribute significantly to the calculation of visibility since measured values are negligible and require long-range transport from the coasts. Therefore in this study, only size-resolved anthropogenic sulphate (SO_4^{2-}) and bulk soot are considered in visibility computations.

[19] The size distributions used have 12 bins ranging from $r_p = 0.005$ μm to $r_p = 20.48$ μm on a doubling scale. All aerosol processes are a function of particle size. The aerosol processes are homogeneous nucleation, coagulation, in-cloud production of aerosol, condensation of water vapor, and H_2SO_4 on preexisting aerosol, gravitational settling, gas-to-particle conversion, emissions and deposition, gas phase, and in-cloud oxydation (Spacek et al., unpublished manuscript, 1999) [*von Salzen et al.*, 2000]. These processes, as well as diffusion, advection, and emissions, are calculated on-line at each model time step. To account for chemical and microphysical processes, all species in NARCM are assumed to be aerosols mixed with sulphates according to their size distribution. However, in this experiment this internal mixing is not performed since only sulphates exist for each size bin.

3.3. Optical Model

[20] While aerosol microphysics and optical properties are required at every model time step in order to compute vertical radiative transfer and energy balance, horizontal visibility is calculated off-line using a standard Mie code and tabulated as a function of composition type, size bin, wavelength, and relative humidity.

[21] This scheme is based on a concentric spherical shell model developed by *Owen and Ackerman* [1981]. Particle types are treated as externally mixed homogeneous materials [*Blanchet and List*, 1983]. This approximation greatly limits the number of possible mixture cases to handle when applied to multicomponent aerosols which could become very complex with the increasing number of species given the likely formation of many compounds and hydrates with varying refractive indices. Although somewhat inconsistent with the internal mixture of aerosol composition assumed in other microphysics and chemical modules of NARCM, the optical properties are dominated by the bulk mass concentration assuming no interaction between pure substance, neglecting possible compounds. However, in the case of insoluble aerosol types (e.g., soil, soot, pollen, etc.) the internal mixture is considered to be a solute concentric shell that surrounds an insoluble kernel. We are fully aware of the complexity of accurately accounting for all processes that affect the state of aerosol mixtures especially in the source region. In this study, the focus on sulphate will reduce this difficulty, although the effect of aerosols on visibility will be somewhat underestimated due to the lack of organics and soil particles in the treatment of aerosols.

[22] In NARCM, optical properties are calculated for all species in each bin and normalized per unit mass concentration of dry aerosol in that size bin. This is done because NARCM prognostic tracers do not include condensed water as an aerosol component, although water uptake is accounted for in microphysical processes such as coagulation, deposition, and chemical alteration. In the Mie calculation, 10 values of relative humidity are evaluated. By interpolating the table to the local relative humidity and weighting the bin by the predicted concentration in NARCM, the variable optical properties consistent with the prognostic aerosol are retrieved. Specifically, the backscattering coefficient in NARCM is obtained from

$$\beta_{\pi_{\mathrm{NARCM}}} = \sum_j \frac{\rho_{\mathrm{air}}}{\rho_j} \sum_i \beta_{\pi_{i,j}} X_{i,j}, \tag{1}$$

where i represents the size bin and j the aerosol species. X is the mass concentration and ρ the density of the aerosol material and ambient air. The value β_π is the backscattering coefficient interpolated for the local relative humidity and obtained from the precalculated table in the Mie code

$$\beta_{\pi_{i,j}} = P_{\pi_{i,j}} \pi \int_{\mathrm{bin}_i} Q_{s_j} r^2 \frac{dN_j(r)}{dr} dr, \tag{2}$$

which is a function of relative humidity, wavelength weighted by the phase function for backscattering P_π. In the present case, only a wavelength of 560 nm is considered. The water uptake is obtained from measurements by *Hänel* [1976]. Refractive indices have been tabulated by *Shettle and Fenn* [1979]. Details of the optical model are discussed more thoroughly by *Blanchet and List* [1983].

4. Experimental Setup

[23] NARCM simulations were performed for 3 days of the 1997 IMADA-AVER campaign, 2, 4, and 14 March. These days were chosen on account of the different daily maximum ozone concentration values. NARCM employs a one-way interactive nested grid structure that increases the horizontal resolution over the region of interest. In this study the modeling domain consists of three nested grids

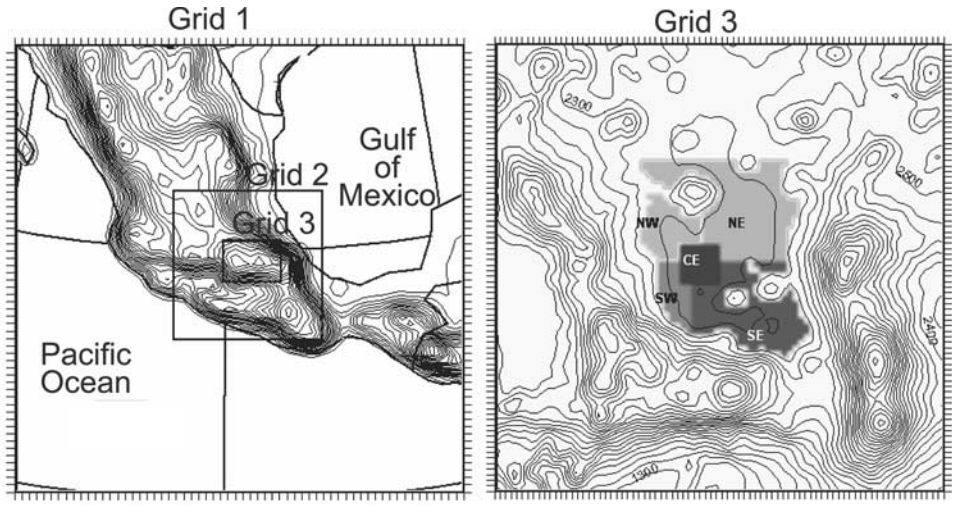

Figure 2. Modeling domain and topography employed by The Northern Aerosol Regional Climate Model (NARCM) with (left) the three nested domains and (right) area of emission sources (all shades) employed in grid 3 and five sampling domains denoted by NW, NE, SE, SW, and CE.

with horizontal grid spacing of 50, 10, and 2 km, respectively, as shown in Figure 2. For the days of interest, each simulation was initialized at 1800 LT (0000 UTC) and run continuously with a 2-week, 7-day, and 24-hour spin-up period, for nested grids 1, 2, and 3, respectively. The coarse grid covers most of central Mexico and parts of the Gulf of Mexico and Pacific Ocean. The inner nested grid provides higher topographic resolution encompassing both Mexico City and the surrounding mountain ranges.

[24] For each grid, atmospheric processes are calculated using 32 vertical grid points between the surface and top level at 19.3 km AGL. Vertical resolution is 50 m close to the surface and decreases progressively until 2100 m and then stays roughly constant. There are 21 levels between the surface and 4 km AGL where the processes responsible for transport and dispersion of pollutants in the boundary layer will be solved. Higher resolutions with 45 vertical levels were tested [*Zuretti*, 1999], and their effect was of secondary importance when compared to the model sensitivity. Successive 12-hour NCEP 2.5° gridded analyses were used to drive the largest domain. Lateral and top boundary points are forced during the simulation period, through the use of the relaxation method of *Davies* [1976]. Forcing at the lateral boundaries is applied on a nine-point sponge zone within each computational domain (see section 3.1).

[25] The sea surface temperature is obtained from the Atmospheric Model Intercomparison Project (AMIP) [*Gates*, 1992].Vegetation in the MCMA consists of forest at the higher elevations surrounding the city and grass, crops, and shrubs at lower elevations. The land descriptor fields needed by CLASS are taken from the table presented by *Verseghy et al.* [1993], which has been modified to represent the region of Mexico City at high resolution (Table 1). The values shown in Table 1 reflect representative characteristics of the different vegetation classes, obtained from exhaustive search of the literature, permitting CLASS to adapt to the region. Topography is specified on the coarse grid from a global 1/6° latitude-longitude data set, while the nested grids are interpolated from a 30-s arc (~1-km resolution) latitude-longitude database [*U.S. Geological Survey*, 1996]. The initial soil moisture is set equal to 25% of the saturation value throughout the soil layer to reflect the dry conditions of the winter season. Soil type was specified as sandy clay loam through the domain. Emissivity, albedo, and roughness length values were set to 0.95, 0.15, and 2 m, respectively, for the metropolitan area.

[26] The Global Emissions Inventory Activity (GEIA) 1985 1-B inventory [*Benkovitz et al.*, 1996], which has two levels and four seasons, was used for the anthropogenic sulphate and SO_2. The SO_2 emissions were adjusted to represent the emissions during the modeled days (2, 4, and 14 March 1997) by scaling them according to annual inventory emission data of Mexico City. The higher-resolution model domain was divided into five subregions that

Table 1. Parameters Associated With Land Cover Categories Used in the Canadian Land Surface Scheme[a]

	Code	Visible Albedo	Near-Infrared Albedo	Roughness Length, m	Max. LAI	Min. LAI	Max. Mass, kg	Rooting Depth, m
Evergreen broadleaf forest	2	0.03	0.23	3.50	10.0	10.0	25.0	5.0
Short grass	4	0.06	0.34	0.02	3.0	3.0	1.5	1.2
Irrigated crop	3	0.06	0.36	0.08	4.0	0.0	2.0	5.0
Thorn shrub	2	0.06	0.32	0.15	3.0	3.0	8.0	5.0

[a]"Code" refers as follows to the vegetation group to which the land cover is assigned: 2, broadleaf tree; 3, crop; 4, grass. LAI, leaf area index; max., maximum; min., minimum.

represent each subregion of the RAMA networks (see Figure 2). These subregions were used to obtain area averages of PM_{10}-simulated concentrations for later comparisons with observed values. For emissions sources, the plume rise formulation of *Briggs* [1975] is applied to take into account the effects of atmospheric stability on the effective heights of the sources. Particles were released within the five subregions near the surface by using a constant release rate of 0.07 tons/day.

[27] The removal of SO_2 from the model ground level by dry deposition is parameterized according to *Padro et al.* [1991]. For aerosol particles the approach described by *Gong et al.* [1997a, 1997b] is used. Concentrations of the tracers are set to zero at the lateral boundaries of the finer grid and at the beginning of the simulation. Thus sources outside the finer grid are neglected, and concentrations are only due to sources within it. Close to the computational boundary walls, within a nine-point sponge zone, this condition acts as a sink of particles, and all model data in the sponge region has no physical significance.

[28] For the purpose of calculating visibility the well-known Koschmieder formula is used [*Koschmieder*, 1924; *Horvath*, 1993; *Horvath and Noll*, 1969]

$$V = \frac{3.912}{\beta_e}, \tag{3}$$

where $\beta_e = \beta_s + \beta_a$ is the extinction coefficient and s and a stand for scattering and absorption, respectively. In terms of horizontal integration the NARCM approximation for the extinction coefficient along inhomogeneous horizontal paths in different directions as a function of time is written as

$$\beta_e = Q_i \frac{\sum_{j=1}^{j=M} \beta_{e_{i,j}} x_{i,j}}{\sum_{j=1}^{j=M} \beta_{e_{i,j}}}, \tag{4}$$

In equation (4), j is the grid range number index used for the summing over all grid points, Q_i is the horizontally integrated coefficient extinction path at direction i, $\beta_{e_{i,j}}$ is the coefficient extinction factor at grid j and direction i, M is the total number of grid points involved in the computation along direction i, and $x_{i,j}$ is the weight factor applied to the inputs. Visibility was calculated using the extinction coefficient averaged over eight grid points in cardinal directions, starting from the grid point close to the airport station. This is consistent with common procedures to determine sector visibility as a function of cardinal direction. The reported visibility is that which represents the larger visibility in a quadrant of the horizon circle.

5. Results

[29] Geopotential heights and wind fields at 500 hPa provided by NCEP analysis and model results are shown in Figure 3. The meteorological conditions during 2 March were characterized by low-pressure systems over northern Mexico (Figure 3a). Over central Mexico, strong southwesterly wind prevailed due to the deep trough over New Mexico and Texas. This pattern gradually gave way to one of high pressure over central Mexico with weak upper-level winds on 4 March, as shown in Figure 3c. On 14 March, somewhat stronger westerly winds aloft developed. On this day the cutoff low drifted slowly northeastward and became entrained into the main branch of the jet stream over the southeastern United States (Figure 3e). The position of the troughs over the United States affected the circulation over central Mexico on each of these days. Transport out of the basin is governed by this synoptic flow pattern, which changed substantially during the study (not shown). The geopotential height and wind field patterns modeled at 500 hPa compare well to the analysis (Figures 3b, 3d, and 3f).

5.1. Meteorological Profiles

[30] The temporal and spatial variations of the mixed layer influence the dispersion and transport of aerosols. For this reason a consistent understanding of the daytime mixed layer is needed to evaluate the evolution of the boundary layer. To demonstrate the ability of the NARCM model to simulate many of the important features of the boundary layer structure and evolution in the MCMA, a comparison of observed and simulated potential temperature profile evolution on 4 March is shown in Figure 4 as a function of height. The growth of the mixed layer was observed often to be similar from one day to the next, and the examination of 1 day is sufficient to show its diurnal evolution.

[31] Here the observed profiles are averaged over the four rawinsonde sites inside the basin and thus represent the temperature evolution of the entire basin atmosphere. The simulated profiles are averages of the profiles at the four grid points nearest to the four observation sites. Inversions in both observations and model results occurred at 0800 LT as expected during the early winter season [*Collins and Scott*, 1993]. The sun warms the air above the surface, creating a shallow mixed layer next to the surface as shown by the 1100 LT profiles. The inversion generally breaks down after sunrise through convective heating. This condition produces a well-mixed planetary boundary layer (PBL) between 1330 and 1630 LT. The features in the boundary layer evolution were captured reasonably well by NARCM, but the strong near-surface inversion observed at 1100 LT was slightly lower by 2 K in the modeled profile (Figure 4). The simulated total cooling in the evening was well represented, and results are consistent with observations despite the relatively low vertical model resolution.

[32] During the dry winter season the basin is dominated by anticyclonic patterns, characterized by light winds and cloudless skies. This condition favored the development of thermally driven local and regional circulations. The boundary layer winds in the Mexico City basin were typically light and easily influenced by small differences in daily synoptic conditions (Figure 3). Comparisons between the observed winds at each profiler site and simulations by NARCM on 4 March are shown in Figure 5. Relatively large near-surface wind speeds occurred during the afternoon and evening at three sites (Chalco, Cuautitlan, and UNAM).The Teotihuacán site was not included since it was too close to the northern computational wall of the high-resolution nested grid, and the modeled values there were affected by spurious gravity wave reflection from the wall.

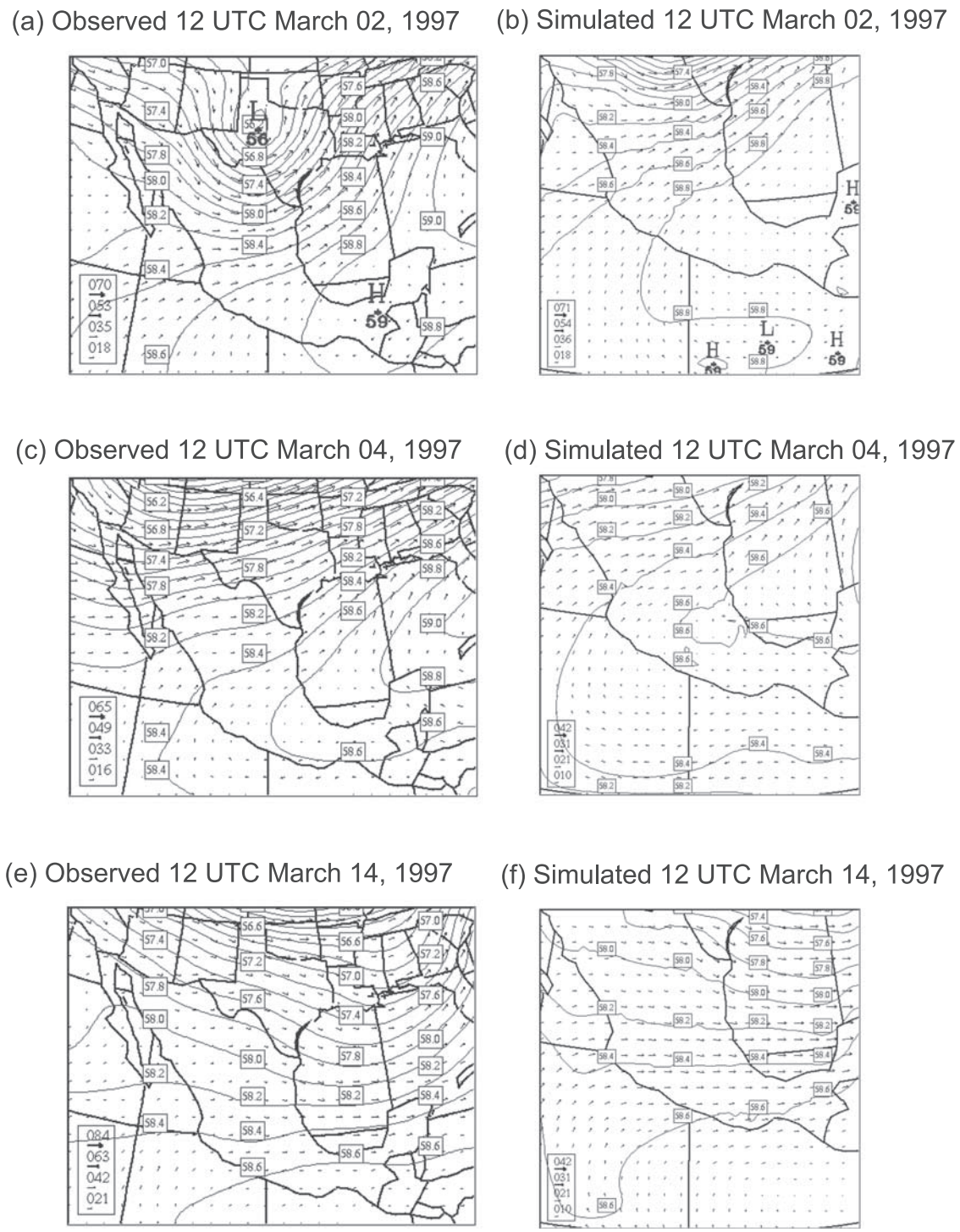

Figure 3. Analyzed geopotential heights (500 hpa) and wind speeds (m/s) for 2, 4, and 14 March 1997 at 1200 UTC. (a, c, e) Observed and (b, d, f) simulated.

[33] The agreement of every station as a function of height and time is remarkably good, demonstrating that the NARCM generates a diurnal cycle of the PBL close to the observations. The largest differences between the observations and the simulations on 4 March were found at the UNAM site, where a sudden shift in wind direction after 1900 LT was not well captured and wind speeds were too weak compared to observations at that site. At the Chalco site the simulation showed an afternoon and evening low-level wind weaker than observed.

5.2. Aerosol Concentration Patterns and Horizontal Transport

[34] The spatial and temporal variation of ozone and particles observed during the IMADA-AVER field campaign varied substantially from day to day at each station

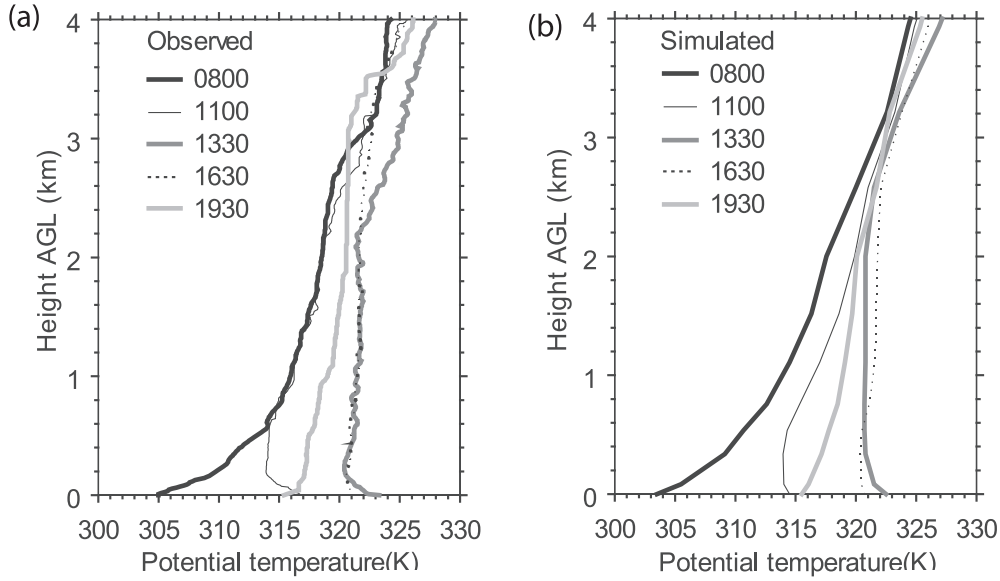

Figure 4. Average of the potential temperature profiles on 4 March 1997, (a) observed (at the four measured sites) and (b) simulated (at the grid points closest to the four sites).

[*Doran et al.*, 1998] in response to changes in circulation and pollutant transport near the surface. Observations of concentrations are only available near the surface. Thus the discussion of the model performance focuses on the near-surface aerosol distributions and transports.

[35] Simulated particle concentration and near-surface winds are shown in Figure 6, as well as observed ozone distribution and wind surface for 2, 4, and 14 March. During 2 March, northeasterly near-surface winds advected aerosols to the southwestern side of the basin (Figure 6a) at 1400 LT. The maximum aerosol concentrations are produced at the southwest of the MCMA, near the highest ozone concentrations. At 1600 LT a convergence of surface winds is produced at about the middle of the MCMA due to stronger southerly winds which appear to be originated from the southeastern gap (Figure 6b). This results in higher particle concentrations shifted to the north compared to the previous simulation at 1400 LT.

[36] On 4 March at 1300 LT, a strong wind with a northerly component produces advection of particles to the south and over the southern mountain range (Figure 6c). Synoptic conditions at this time were important to the export of particles out of the basin. This was evident from inspection of vertical cross sections of particle concentrations (not shown), which is in agreement with past studies [*Fast and Zhong*, 1998]. At 1700 LT, ventilation was evident, and a dilution of particles over the southeastern mountain range was produced. This is to be contrasted with the behavior of observed ozone which does not appear to be affected by ventilation and was only slightly advected to the south (Figure 6d).

[37] During the afternoon of 14 March at 1400 LT, the near-surface winds were easterly over much of the basin except in the southeast portions, where the winds were southerly. Aerosols were advected predominantly to the northwestern side of the basin, as shown in Figure 6e. Because of the intensification and propagation of the southerly flows into the middle basin at 1600 LT (Figures 6e and 6f), aerosols reached the northwestern sector. At these times of simulation the maximum of particle concentrations was located near the observed maximum ozone concentrations.

[38] In general, the model exhibits good ability in reproducing the main features of local surface wind patterns. Particle concentrations respond to changes in local circulation as expected; however, observed ozone concentrations are not always in synchronicity with these particle distributions. This indicates that processes other than advection are probably at work as far as the evolution of ozone spatial distribution and generation through the MCMA is concerned.

5.3. Particulate Matter 10 (PM_{10}) and Visibility

[39] It is common practice to classify aerosol particles in several size ranges or modes. Particles in the so-called accumulation mode (0.1–1 μm) are produced by the coagulation of smaller particles and by the heterogeneous condensation of gas vapor onto existing aerosol particles [*Pruppacher and Klett*, 1997]. These particles are very effective in reducing visibility. Two sources of error become apparent in NARCM simulation of aerosols for the accumulation mode. The first one comes from computational errors of the semi-Lagrangian scheme at low spatial resolutions (50–100 km). The second one comes from an insufficient number of size bins needed to resolve the distribution spectra of particles. This results in a systematic underestimation of their number concentration (Spacek et al., unpublished manuscript, 1999). One coagulation scheme proposed by *Jacobson et al.* [1994] has been used to addresses this problem at higher spatial resolutions.

[40] The approach taken here was to subdivide the size spectrum into subintervals, so as to increase the resolution only in the coagulation process. The resolution was increased from 12 to 36 size intervals. This method increased the concentration in the accumulation mode by ~1 order of magnitude. Figure 7 shows a daily average of number size

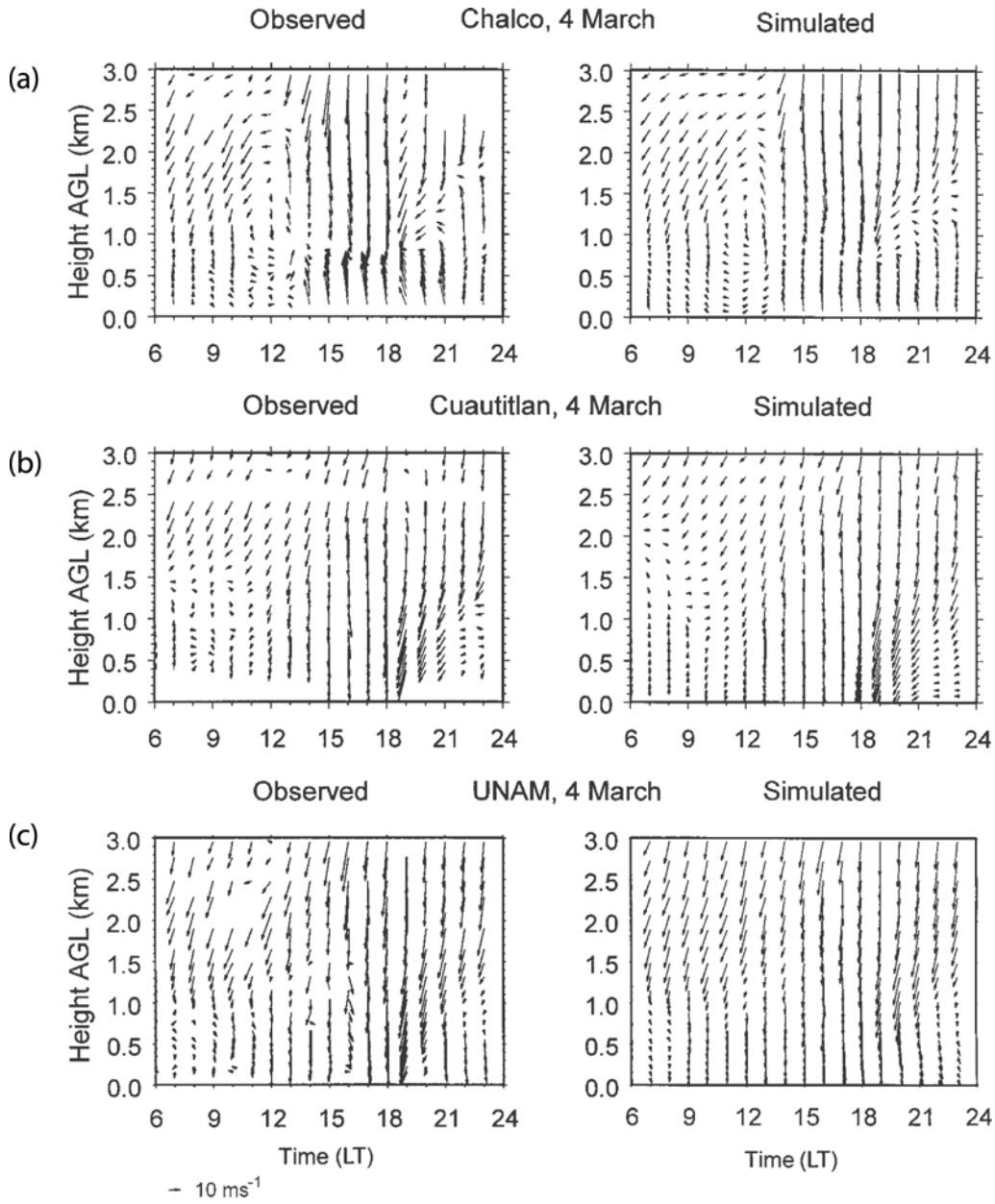

Figure 5. (left) Observed and (right) simulated horizontal wind vector profiles at (a) Chalco, (b) Cuautitlan, and (c) UNAM, on 4 March 1997.

and volume size distributions for 2 March. Additionally, Figure 7b shows how significant differences exist between the old and newer schemes. The importance of such differences becomes apparent when visibility calculations are performed. Similar distributions for sulfates have been measured in the MCMA by M. Moya et al. (Characterization of size-differentiated inorganic composition of aerosols in Mexico City, submitted to *Atmospheric Environment*, 2003) where the accumulation mode is found to be around 0.3 μm and is comparable to the simulated size distributions. It is worth mentioning here that very little information about aerosol size distributions for organic and inorganic compounds currently exists for the MCMA.

[41] To estimate the ability of the model to replicate spatial and temporal variation of fine particles, hourly observed PM_{10} concentrations at the ground averaged over each station group and simulated concentration of PM_{10} within each of the five MCMA sampling domains are shown in Figure 8 for each simulated day. PM_{10} concentrations exceeded the Mexican air quality standard of 150 $\mu g/m^3$ in almost all station groups for the 3 days (Figures 8a, 8c, and 8e). This is typical of the MCMA during winter [*Collins and Scott*, 1993]

[42] On 2 March, as seen in Figure 6, particles were advected primarily to the southwest of the MCMA after 1400 LT, decreasing the fraction of particles in the southeast and northeast of the basin (Figure 8a). The smallest fraction of particles on 4 March occurred in the southeast section (Figure 8c). Although maximum values are observed during the morning and afternoon at other stations, in the south-

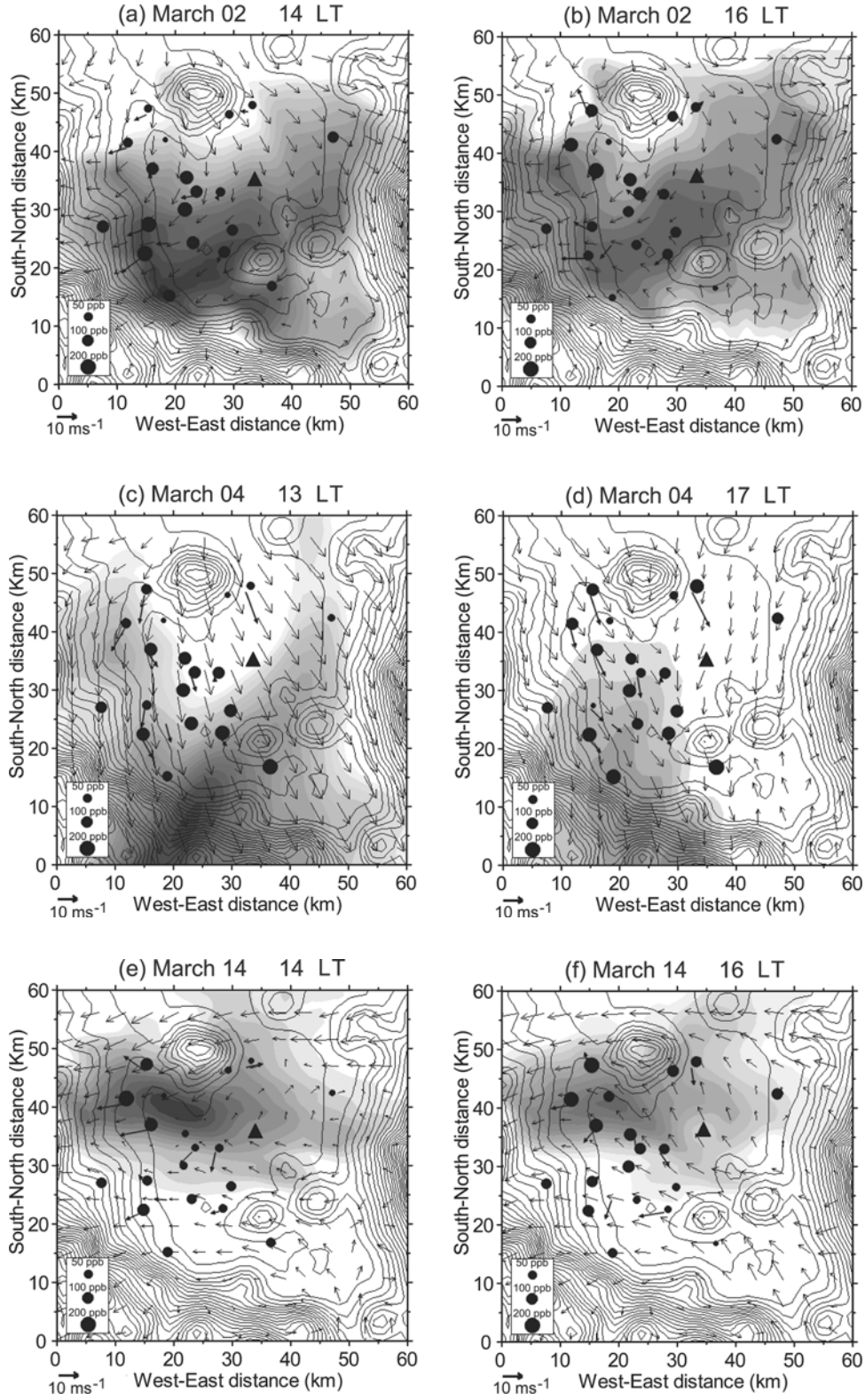

Figure 6. Simulated near-surface winds and particle concentrations (shaded areas) over a subarea of the third nested grid at (a) 1400 and (b) 1600 LT for 2 March, (c) 1300 and (d) 1700 LT for 4 March, and (e) 1400 and (f) 1600 LT for 14 March. Contours represent topography (50-m intervals), solid circles denote the magnitude of observed ozone concentrations, and the solid vectors are the observed profiles near surface winds. Triangles denote the airport location in Figures 6a–6d.

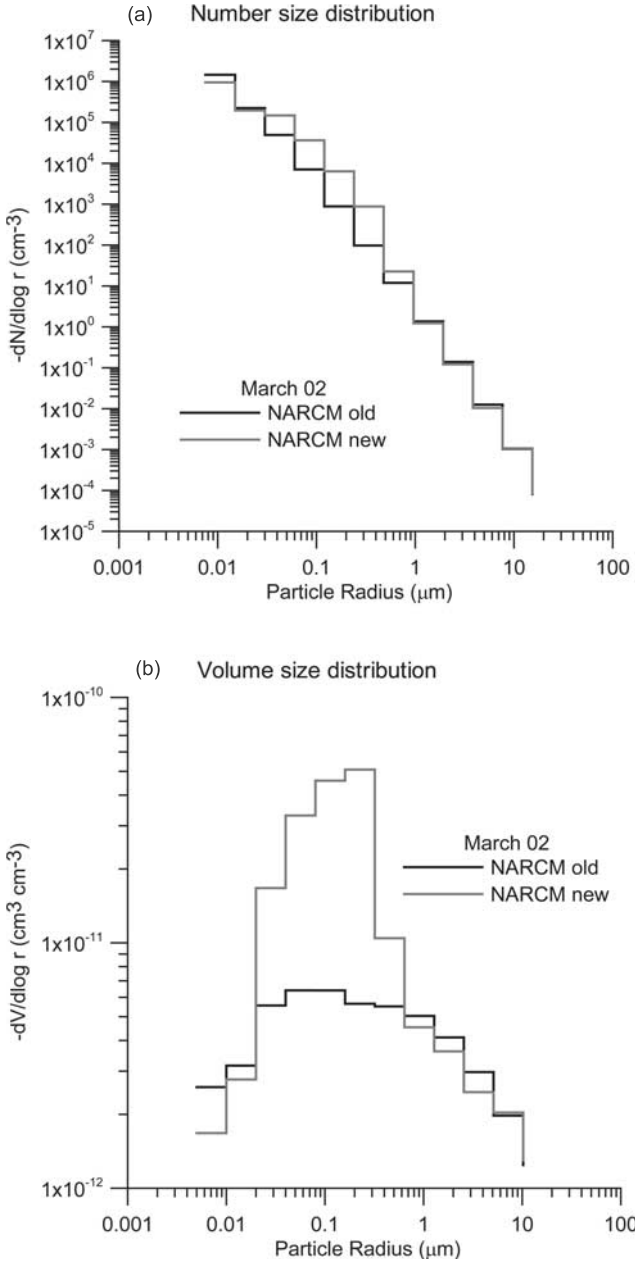

Figure 7. (a) Number size and (b) volume size distribution of aerosol particles for 2 March.

western area, the largest fractions of particles occurred during afternoon. On 14 March a maximum is seen in the central region and to the southwest of the MCMA during the afternoon (Figure 8e). In general, measurements taken throughout the day did not reveal a day-to-day buildup of particles, but afternoon ventilation followed by increasing concentrations during evening (Figure 8a, 8c, and 8e).

[43] As expected, the general concentration is underestimated mostly due to lack of organics and soil particles. It is also obvious that the double peaks have only weak amplitude due to the lack of urban chemistry in the model. However, the regional relative distribution of concentration is captured well by the model.

[44] Table 2 shows a comparison between observed $PM_{2.5}$ concentrations and those modeled by NARCM. In both sets except for 14 March a larger particle concentration on the Netzahualcóyotl (NET) station located east of the MCMA is found consistently. This can be attributed to a characteristic wind pattern that shifted from northwesterly winds during 2 and 4 March to southeasterly winds during 14 March (see Figure 6). The order of magnitude of modeled data is similar to that provided by observational data from *Edgerton et al.* [1999]. The observed intersite variation of measured concentration of $PM_{2.5}$ is $\sim$25 $\mu g/m^3$ which is also similar to that shown by the model.

[45] Aerosol concentrations are highly variable in space and time (see Figure 6). Integration along various horizontal directions leads to highly variable visibility, as data from the Mexico City airport shows. The horizontal visibility, defined by the sector with highest values, is a function sensitive to aerosol amount along the path, its size distribution, humidity, and the material composition of aerosol distributions within the basin.

[46] Figure 9 shows a comparison of daily observed and simulated visibility for March 2, 4, and 14. It varies strongly in amplitude, between 4 and 20 km, during these days. It also reflects the air circulation and urban activities. Figure 9 shows that visibility in the MCMA is sensitive to direction in the horizontal plane, particularly in the middle of the day when concentration is heterogeneous and mixing is increasing. The gradual development of the mixed layer (Figure 4) is responsible for the steady increase of visibility in the afternoon. In the morning and at night the particles are trapped near the surface by the thermal inversion (Figure 4), resulting in poor visibility. In the afternoon, with the growing mixed layer and increasing vertical turbulence, the aerosol becomes drier and more diluted. Figure 9a shows the effect of resolved bin size in the computation of aerosols. For coagulation computations the 12 size bin distribution (NARCM old) shows values of visibility around 5 km at noon while from the 36 size bin distribution (NARCM new), visibility is $\sim$8 km closer to observed (9 km). Figure 9b shows the dependence on cardinal direction of visibility. The best visibility is found on the east and north directions as expected from Figure 6a for 2 March around 1400 LT. Figures 9c and 9d show similar behavior to 2 March. This is a significant achievement given that these computations are physically based without relying on empirical or statistical curve fitting. The differences against observations can be attributed in large part to the lack of size-resolving coagulation computation but also to the missing aerosol species like organics (black and organic carbon) and soil components.

[47] The comparison of visibility is a difficult test on aerosol models. It is an integrated index of the state of the aerosol and needs to be carefully monitored and documented with other related variables (aerosol size spectra, composition, water uptake, moisture content, and concentration as time series) in future campaigns on air quality.

6. Summary and Conclusions

[48] Proper simulation of aerosol evolution requires a good representation of emission at the source itself where transformation (oxidation, coagulation, and deposition) processes are most effective due to high concentration of particles and gaseous precursors. The evolution of atmo-

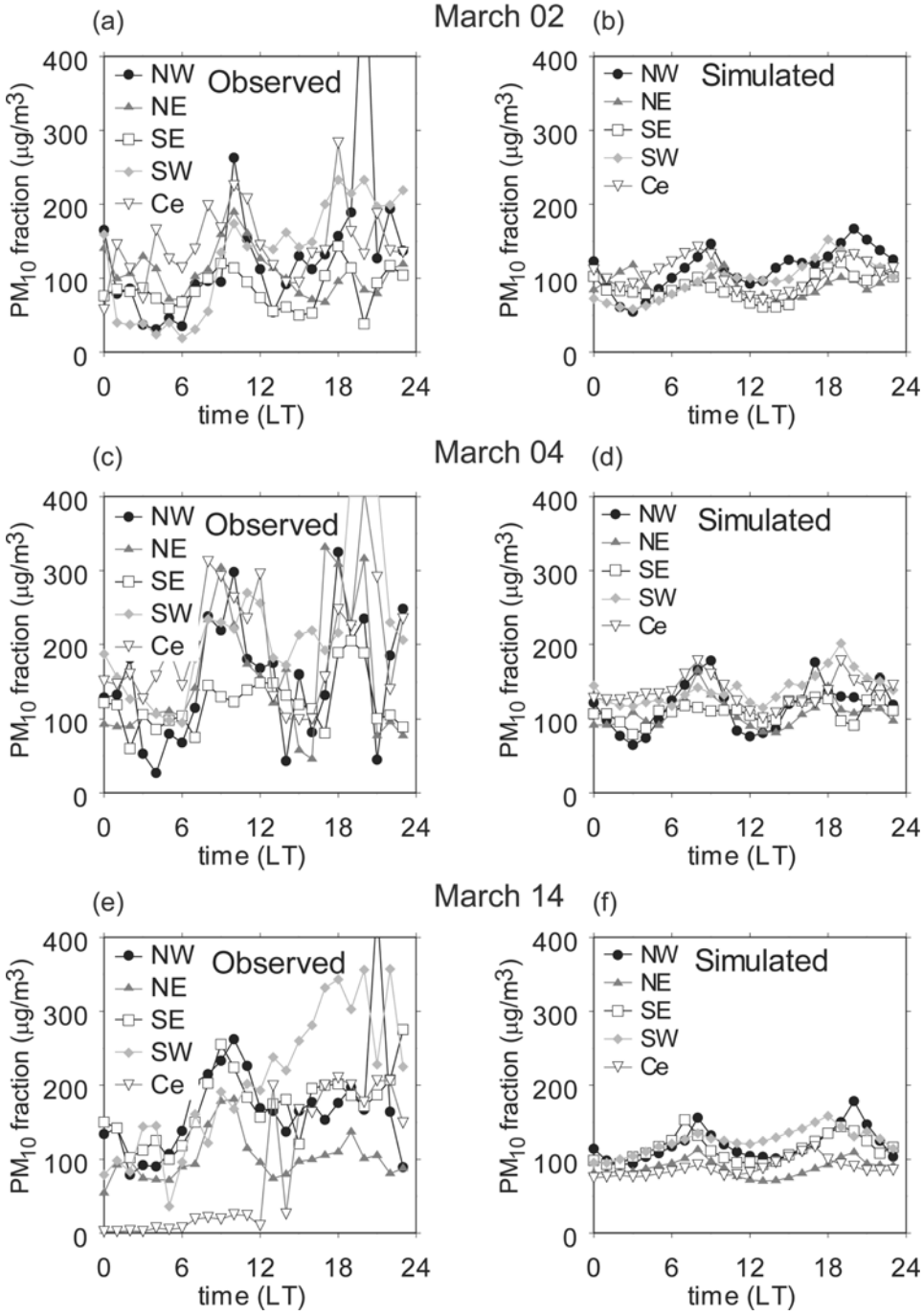

Figure 8. Daily mean variation of particulate matter 10 (PM_{10}) (a, c, e) observed in each station group and (b, d, f) simulated in each sampling domain for 2, 4, and 14 March. (Quantities are area averaged within each subregion of Figure 2 of the finer grid.)

spheric visibility offers a valuable test for aerosol microphysics and optical properties. This helps evaluate aerosol and atmospheric models. To address this issue in some detail, we performed a simulation with NARCM using a horizontal grid spacing of 2 km, over the densely populated region of Mexico City during 3 days of the IMADA-AVER campaign. Although the model is deficient from the point of view of air quality, it is an important step in applying and verifying complex models such as NARCM at urban scales. Such a tool permits the prognostic computation of visibility on a physical basis.

[49] We were able to compare hourly radiosonde profiles at all measuring stations used during the 3 days, 2, 4, and 14 March 1997. We investigated the simulations of urban sulphate aerosol components calculated during these days. The observed evolution of the PBL agrees remarkably with the simulations (temperature, moisture, and wind profiles; not shown).

Table 2. Twenty-Four-Hourly Average Particulate Matter 2.5 ($PM_{2.5}$) Concentrations Measured and Simulated at Different Sites of the RAMA Stations[a]

	2 March		4 March		14 March	
Site	Obs. $PM_{2.5}$	Sim. $PM_{2.5}$	Obs. $PM_{2.5}$	Sim. $PM_{2.5}$	Obs. $PM_{2.5}$	Sim. $PM_{2.5}$
TLA	27	40	35	43	54	44
MER	32	36	49	52	35	28
PED	23	34	32	54	26	46
XAL	41	29	66	38	53	28
NET	54	53	83	59	44	53
CES	38	28	55	39	32	41

[a]Measurements are in $\mu g/m^3$. Obs., observations; Sim., simulations.

[50] By investigating the structure and evolution of the PBL and its relation to the large-scale flow, we examined the vertical transport, mixing, and production of aerosol layers within the basin atmosphere. The case of Mexico City is strongly influenced by orographic flow, which the model captured well at a resolution of 2 km. An integrated measurement and modeling analysis is presented which helps describe the characteristics of the wind fields and the meteorological processes together with an explicit sulphate aerosol model. The basic results of our simulation are qualitatively similar to the three wind patterns, local, regional, and synoptical, described by *Bossert* [1997]. They are considered representative of the circulation in the region. In fact, the growth of the mixed layer was often comparable from one day to the next, and examination of one representative day was sufficient to illustrate the general features of the daily mixed layer evolution. However, the relative prominence of each pattern differed significantly from day to day, making it more difficult to describe the winds on a "typical" day by looking only at a single case. The three cases provide a wider range of conditions for testing the model.

[51] Observations of PM_{10} throughout the day did not show a day-to-day buildup of particles but, rather, afternoon ventilation followed by increasing concentrations during evening and morning. Maximum particle concentrations are produced in the southwest and southeast sectors of the city when northerly winds develop with heating of the plateau and generates valley winds and anabatic flow on mountain sides. When deep boundary layer draws air through the southeastern gap in the mountains, most of the particles are transported toward the northwest sector of the city.

[52] The most important accomplishment of this study is the calculation of visibility at the airport of Mexico City using physically based aerosols and an optical model in a regional climate model. Time series of directional visibility show their dependence on the horizontal distance, azimuthal direction, time, aerosol concentrations, size distribution, and humidity. Visibility is sensitive to many processes in the aerosol and account for the regional distribution via directional integration in the horizontal plane.

[53] Decrease or increase in the constituents of the visibility calculations are complex and depend on many

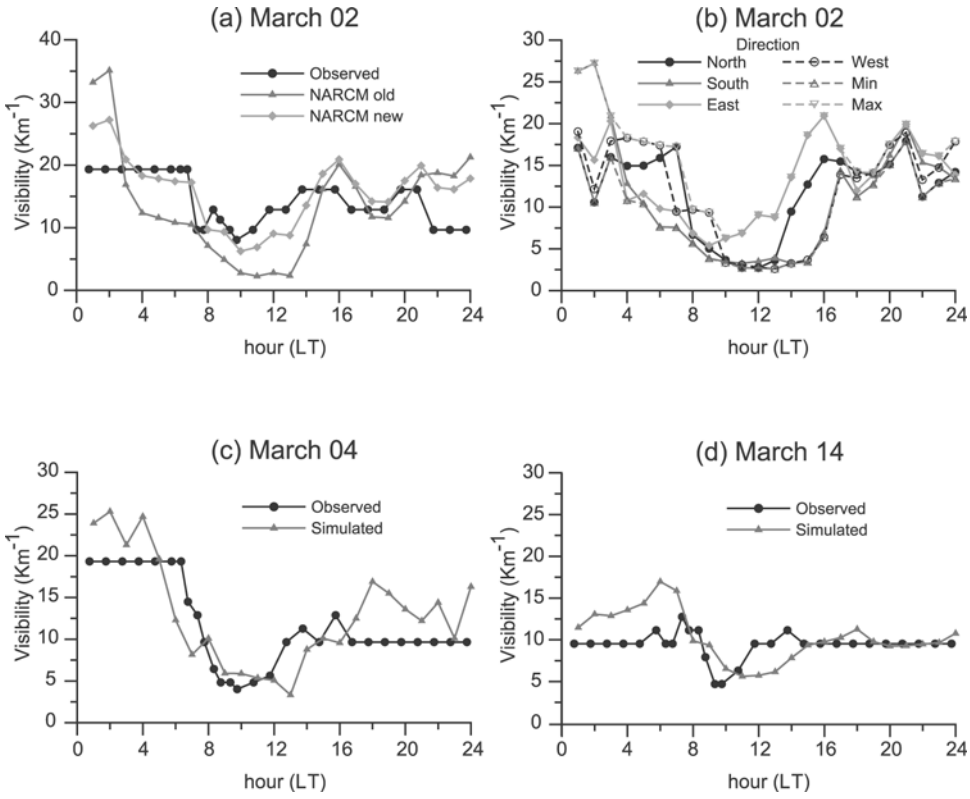

Figure 9. Observed and calculated visibility for (a) 2 March, (c) 4 March, and (c) 14 March. Calculations with the old and new coagulation scheme are shown in Figure 9a. For 2 March the directional visibility is shown in Figure 9b, where N, S, E, and W, are the north, south, east, and west directions, respectively.

factors such as the availability of oxidants, internally versus externally mixed aerosols, hygroscopicity, mixture, ambient relative humidity, temperature, transport pattern of aerosol components, and precursor emissions. An important result out of this study with NARCM is that in order to obtain realistic visibility calculations, a minimum requirement is to have a properly resolved size spectrum for coagulation computations. Despite a higher computational cost, it is desirable to increase the number of subintervals to obtain better rates and therefore proper accumulation simulations. The use of sulphates and soot in visibility calculations was considered necessary to simplify an already very complex calculation. This should be regarded as a first step in understanding the model's behavior when compared to observations of visibility. In spite of the limited amount of data and model limitations, it is clear that the model is able to capture the essential features required for visibility simulations and provides a guide for future developments.

[54] **Acknowledgments.** We are grateful to Servicios a la Navegacion en el Espacio Aereo Mexicano (SENEAM) for providing visibility data at the Mexico City airport. We also acknowledge two anonymous reviewers whose comments contributed to improving the manuscript.

References

Benkovitz, C. M., M. T. Scholtz, J. Pacyna, L. Tarrasón, J. Dignon, E. C. Voldner, P. A. Spiro, J. A. Logan, and T. E. Graedel, Global gridded inventories of anthropogenic emissions of sulphur and nitrogen, *J. Geophys. Res.*, *101*, 29,239–29,253, 1996.

Blanchet, J.-P., and R. List, Estimation of optical properties of Arctic haze using a numerical model, *Atmos. Ocean*, *21*, 444–465, 1983.

Borja-Aburto, V. H., D. P. Loomis, S. I. Bangdiwala, C. M. Shy, and R. A. Rascon-Pacheco, Ozone, suspended particulates, and daily mortality in Mexico City, *Am. J. Epidemiol.*, *145*(3), 258–268, 1997.

Bossert, J. E., An investigation of flow regimes affecting the Mexico City region, *J. Appl. Meteorol.*, *36*, 119–140, 1997.

Briggs, G. A., Comparison of the trajectories of rising plumes with theoretical empirical models, *Atmos. Environ.*, *9*, 455–462, 1975.

Caya, D., and R. Laprise, Semi-implicit semi-Lagrangian regional climate model: The Canadian RCM, *Mon. Weather Rev.*, *127*, 341–362, 1999.

Collins, C. O., and S. L. Scott, Air pollution in the Valley of Mexico, *Geogr. Rev.*, *83*, 119–133, 1993.

Davies, H. C., A lateral boundary formulation for multi-levels prediction models, *Q. J. R. Meteorol. Soc.*, *102*, 405–418, 1976.

Denis, B., R. Laprise, and D. Caya, Sensitivity of a regional climate model to the resolution of the lateral boundary conditions, *Clim. Dyn.*, *20*, 107–126, 2003.

Doran, J. C., et al., The IMADA-AVER boundary-layer experiment in the Mexico City area, *Bull. Am. Meteorol. Soc.*, *79*, 2497–2508, 1998.

Edgerton, S. A., et al., Particulate air pollution in Mexico City: A collaborative research project, *J. Air Waste Manage. Assoc.*, *49*, 1221–1229, 1999.

Fast, J. D., and S. Zhong, Meteorological factors associated with inhomogeneous ozone concentrations within the Mexico City basin, *J. Geophys. Res.*, *103*, 18,927–18,946, 1998.

Gates, W. L., AMIP: The Atmospheric Model Intercomparison Project, *Bull. Am. Meteorol. Soc.*, *73*, 1962–1970, 1992.

Georgi, F., Simulation of regional climate using a limited area model nested in a General Circulation Model, *J. Clim.*, *3*, 941–963, 1990.

Gong, S. L., L. A. Barrie, and J.-P. Blanchet, Modeling sea-salt aerosols in the atmosphere: 1. Model development, *J. Geophys. Res.*, *102*, 3805–3818, 1997a.

Gong, S. L., L. A. Barrie, J. M. Prospero, D. L. Savoie, G. P. Ayers, J.-P. Blanche, and L. Spacek, Modeling sea-salt aerosols in the atmosphere. 2: Atmospheric concentrations and fluxes, *J. Geophys. Res.*, *102*, 3819–3830, 1997b.

Gong, S. L., et al., Canadian Aerosol Module: A size-segregated simulation of atmospheric aerosol processes for climate and air quality models: 1. Module development, *J. Geophys. Res.*, *108*(D1), 4007, doi:10.1029/2001JD002002, 2003.

Guzman, F., and G. E. Streit, Mexico City air quality research initiative, in *Air Pollution '93*, edited by P. Zannetti et al., pp. 599–609, Comput. Mech., Billerica, Mass., 1993.

Hänel, G., The properties of atmospheric aerosol particles as functions of the relative humidity at thermodynamic equilibrium with the surrounding moist air, *Adv. Geophys.*, *19*, 73–188, 1976.

Horvath, H., Atmospheric light absorption—A review, *Atmos. Environ.*, *27*(*Part A*), 293–317, 1993.

Horvath, H., and K. E. Noll, The relationship between atmospheric light scattering coefficient and visibility, *Atmos. Environ.*, *3*, 543–552, 1969.

Jacobson, M. R., R. Turco, E. Jensen, and O. Toon, Modeling coagulation among particles of different composition and size, *Atmos. Environ.*, *28*, 1327–1338, 1994.

Jauregui, E., Local wind and air pollution interaction in the Mexico basin, *Atmosfera*, *1*, 131–140, 1988.

Jauregui, E., Heat island development in Mexico City, *Atmos. Environ.*, *31*, 3821–3831, 1997.

Koschmieder, H., Theorie der horizontalen sichtweite, *H. Beit. Phys. Freien. Atm.*, *12*, 171–181, 1924.

Laprise, R., D. Caya, G. Bergeron, and M. Giguere, The formulation of Andre Robert MC2 (Mesoscale Compressible Community) model, *Atmos. Ocean*, *35*, 195–220, 1997.

McFarlane, N. A., G. J. Boer, J.-P. Blanche, and M. Lazare, The Canadian Climate Centre second generation circulation model and its equilibrium climate, *J. Clim.*, *5*, 1013–1044, 1992.

Molina, M. J., and L. T. Molina, Integrated strategy for air quality management in the Mexico City metropolitan area, *MIT-IPURGAP Rep. 7*, 126 pp., Mass. Inst. of Technol., Cambridge, Mass., 2000.

Oke, T. R., G. Zeuner, and E. Jauregui, The surface energy balance in Mexico City, *Atmos. Environ.*, *26*(*Part B*), 433–444, 1992.

Owen, B. T., and T. P. Ackerman, Algorithms for the calculation of scattering by stratified spheres, *Appl. Opt.*, *20*(20), 3657–3660, 1981.

Padro, J., H. H. Neumann, and G. D. Hartog, An investigation of the ADOM dry deposition module using summertime 03 measurements above a deciduous forest, *Atmos. Environ., Part A*, *25*, 1689–1704, 1991.

Pruppacher, H. R., and J. D. Klett, *Microphysics of Clouds and Precipitation*, 2nd ed., 954 pp., Kluwer Acad., Norwell, Mass., 1997.

Raga, G. B., T. Castro, and D. Baumgardner, The impact of megacity pollution on local climate and implications for the regional environment: Mexico City, *Atmos. Environ.*, *35*, 1805–1811, 2001.

Romieu, I., M. Ramirez, F. Meneses, D. Ashley, S. Lemire, S. Colome, K. Fung, and M. Hernandez-Avila, Environmental exposure to volatile organic compounds among workers in Mexico City as assessed by personal monitor and blood concentrations, *Environ. Health Perspect*, *107*(7), 511–515, 1999.

Seinfeld, J. H., and S. N. Pandis, *Atmospheric Chemistry and Physics: From Air Pollution to Climate Change*, John Wiley, Hoboken, N.J., 1998.

Shettle, G. E., and K. Fenn, Models for the aerosols of the lower atmosphere and the effects of humidity variations on their optical properties, *Environ. Res. Pap. 676, AFGL-TR-79-0214, NTIS AD-A085 951/2*, 94 pp., Air Force Geophys. Lab., Bedford, Mass., 1979.

U.S. Geological Survey, GTOPO30: Global 30 Arc-Second Elevation Data Set, http://edcdaac.usgs.gov/gtopo30/gtopo30.html, EROS Data Cent., Sioux Falls, S.D., 1996.

Verseghy, D. L., CLASS—A Canadian land surface scheme for GCMs, I. Soil model, *Int. J. Climatol.*, *11*, 111–133, 1991.

Verseghy, D. L., N. A. McFarlane, and M. Lazare, CLASS—A Canadian land surface scheme for GCMs, II. Vegetation model and coupled runs, *Int. J. Climatol.*, *13*, 347–370, 1993.

von Salzen, K., H. G. Leighton, P. A. Ariya, L. A. Barrie, S. L. Gong, J.-P. Blanchet, L. Spacek, U. Lohmann, and L. I. Kleinman, Sensitivity of sulphate aerosol size distributions and CCN concentrations over North America to SO*x* emissions and H_2O_2 concentrations, *J. Geophys. Res.*, *105*, 9741–9765, 2000.

Whiteman, C. D., S. Zhong, X. Bian, J. D. Fast, and J. C. Doran, Boundary layer evolution and regional-scale diurnal circulations over the Mexico basin and Mexican plateau, *J. Geophys. Res.*, *105*, 10,081–10,102, 2000.

Yakimiw, E., and A. Robert, Validation experiments for a nested grid-point regional forecast model, *Atmos. Ocean*, *28*, 466–472, 1990.

Zhang, G. J., and N. A. McFarlane, Sensitivity of climate simulations to the parameterization of cumulus convection in the Canadian Climate Centre General Circirlation Model, *Atmos. Ocean*, *33*, 407–446, 1995.

Zuretti, F., Simulations de la circulation atmosphérique dans le bassin de Mexico à l'aide du modèle NARCM, M.Sc. thesis, U. du Québec á Montréal, Montreal, Quebec, Canada, 1999.

J.-P. Blanchet and R. Munoz-Alpizar, Department of Earth and Atmospheric Sciences, University of Quebec at Montreal, Montreal, Quebec, Canada, H3C 3P8. (blanchet.jean-pierre@uqam.ca; rodrigo@sca.uqam.ca)

A. I. Quintanar, Instituto Mexicano del Petroleo, 152 Eje Central Norte, Mexico D.F. 07730, Mexico. (aquintan@imp.mx)